JOURNAL OF SPACECRAFT AND ROCKETS
Vol. 47, No. 5, September–October 2010

Postflight Aerothermal Analysis of Stardust Sample Return Capsule

Kerry A. Trumble*
NASA Ames Research Center, Moffett Field, California 94035
Ioana Cozmuta† and Steve Sepka‡
ELORET Corporation, Sunnyvale, California 94086
Peter Jenniskens§
SETI Institute, Mountain View, California 94043
and
Michael Winter¶
NASA Ames Research Center, Moffett Field, California 94035

DOI: 10.2514/1.41514

The reentry of the Stardust sample return capsule was captured by several optical instruments through an observation campaign aboard the NASA DC-8 airborne observatory. Flow environments obtained from computational fluid dynamics solutions are loosely coupled with material response modeling to predict the surface temperature and the observed continuum emission of Stardust throughout the reentry. The calculated surface temperatures are compared with the data from several spectral instruments onboard the airborne observatory, including the ECHELLE (echelle-based spectrograph for the crisp and high efficient detection of low light emission) camera and conventional spectrometer in Czerny–Turner configuration. The ECHELLE camera recorded spectral intensity at a period in the trajectory before peak heating. The graybody curves corresponding to the average and area-averaged surface temperatures predicted by the computational fluid dynamics and material response coupled simulation have excellent agreement with the recorded data at altitudes lower than 74 km. At these altitudes, the computational fluid dynamics and material response coupling agrees with the surface temperature to within 50 K. The computational fluid dynamics calculation without the material response modeling overestimates surface temperatures because it does not take into account such things as ablation. The overprediction of the computational fluid dynamics and material response simulated surface temperature early in the trajectory coincides with high-emission intensity lines corresponding to thermal paint products. The presence of paint on the heat shield could have contributed to the lower observed surface temperatures and could explain the overprediction by the simulated data, which does not account for the paint. The average surface temperatures resulting from the spectrometer in Czerny–Turner configuration telescope analysis agree to within less than 5% with the average surface temperatures predicted by the material response. This observation period included the point of peak heating. The calculated flux based on the surface temperature agrees well with the observed flux. Surface temperature is one of the critical parameters used in the design of thermal protection systems, because it is an indicator of material performance. The coupled computational fluid dynamics and material response approach employed in the present analysis increases confidence for future missions such as the crew exploration vehicle Orion.

Nomenclature

A = surface area, m^2
B = Planck's blackbody flux, 10–12 $W/m^2/nm$
c = speed of sound, m/s
D = distance from the airborne observatory to the Stardust sample return capsule, m
g = graybody flux, 10–12 $W/m^2/nm$
h = Planck's constant, J · s
k = Boltzmann's constant, J/K
T = temperature, K
V = freestream velocity, km/s
ε = emissivity
λ = wavelength, nm
ρ = freestream densitykg/m^3

Presented as Paper 1201 at the 46th AIAA Aerospace Sciences Meeting and Exhibit, Reno, NV, 7–10 January 2008; received 20 October 2008; accepted for publication 26 April 2009.

*Research Scientist, Reacting Flow Environments Branch, Mail Stop 230-2. Member AIAA.
†Senior Research Scientist, Reacting Flow Environments Branch, Mail Stop 230-3. Member AIAA.
‡Senior Research Scientist, Thermal Protection Materials and Systems Branch, Mail Stop 234-1. Member AIAA.
§Research Scientist, Principal Investigator, Carl Sagan Center, 515 North Whisman Road. Member AIAA.
¶Senior Research Scientist, University Affiliated Research Center, Mail Stop 230-3. Member AIAA.

I. Introduction

THE Stardust sample return capsule (SRC) was launched in February 1999 on a mission to retrieve samples of interstellar dust from the tail of comet Wild-2. Stardust returned to Earth in January 2006 entering the atmosphere with a velocity of 12.8 km/s, the fastest Earth reentry and highest-energy reentry of any artificial vehicle to date. Several instruments aboard the NASA DC-8 airborne observatory captured the reentry [1]. This paper compares broadband flux and continuum spectral emission measured by these instruments [2,3] with the emission expected from the surface temperature calculated using loosely coupled aerothermodynamic computational fluid dynamics (CFD) and material response simulations along the estimated flight trajectory (EFT). Spectral data were recorded using a miniature echelle spectrograph called ECHELLE (echelle-based spectrograph for the crisp and high efficient detection of low light emission), developed specifically for the Stardust observation

campaign to obtain optical spectroscopy at high spectral resolution [2]. These data were obtained during a period of reentry before peak heating. Calculated data were also compared with the results of Winter and Herdrich [3], who captured a large portion of the reentry using an Acton 300i laboratory spectrometer in Czerny–Turner configuration (slit-based spectrometer called SLIT) with a focal length of 300 mm.

The Stardust observation data provide a rare opportunity to compare simulation with flight data in the hypervelocity regime. Furthermore, the thermal protection system (TPS) on the heat shield of Stardust was phenolic impregnated carbon ablator (PICA), which, at the time of this writing, was the primary candidate heat-shield material for NASA's Orion Crew Exploration Vehicle (CEV) Project. Because Stardust had an entry velocity similar to lunar return and employed PICA as the TPS material, its postflight analysis is directly relevant to the CEV Project.

The aerothermal environment of Stardust is modeled through CFD with the code Data Parallel Line Relaxation (DPLR) [4]. The CFD provides predictions for surface shear, pressure, temperature, heat transfer, and integrated heat load. The surface recession, char layer, density variations, and surface temperature are predicted with the material response code Fully Implicit Ablation and Thermal Analysis (FIAT) [5]. The surface temperatures obtained through these tools will be compared with the observation data.

The objective of this paper is to validate the predictions of the surface temperature of Stardust throughout its reentry trajectory to Earth's surface. Section II of this paper discusses the flow conditions of the EFT. Section III describes the CFD methodology used to simulate the flowfield around the Stardust capsule. The aerothermal environment as computed from CFD simulations is used as input to the material response code over the heat shield to calculate surface temperatures. Sections IV and V present and discuss the results of the CFD analysis, independently and coupled with the material response code and the comparison of surface temperatures with the observational data.

A. Flow Conditions

The Stardust capsule is a 60-deg-half-angle spherically blunted cone with a nose radius of 0.2286 m and a shoulder radius of 0.01905 m. The entry of Stardust was nearly ballistic [6], and therefore the capsule is represented in the CFD as two-dimensional and axisymmetric, which enables a quick turnaround in computational time. The profile of Stardust and its hyperbolic grid, which will be discussed later, are shown in Fig. 1. The wall boundary condition is fully catalytic radiative equilibrium. No blowing is being modeled.

The CFD solutions calculated along the EFT [6] observed by the capsule are listed in Table 1. The radiative heating is neglected in this analysis because it constitutes less than 10% of the peak heat flux; the convective heating is the dominant source of heating. Although the velocity is higher, the shock layer is thin and keeps the radiative heating low. The peak-heating point is at $t = 51$ s ($t = 0$ s is when the capsule first enters the atmosphere), and the velocity is 10.9 km/s, the mass density is 2.11×10^{-4} kg/m^3, and the freestream temperature is 235 K. The maximum convective heat flux at the peak-heating time point is 942 W/cm^2.

The ECHELLE instrument collected spectroscopic data between 368 and 872 nm from $t = 34$ to 44 s. It is estimated that $t = 34$ s is on the cusp between the continuum and noncontinuum regimes, with a Knudsen number of approximately 0.005 based on the diameter of the capsule. At $t = 34$ s the velocity is 12.4 km/s, the mass density is 1.27×10^{-5} kg/m^3, and the freestream temperature is 217.6 K. At $t = 44$ s the velocity is 11.9 km/s, the mass density is 7.72×10^{-5} kg/m^3, and the freestream temperature is 224.1 K. The SLIT instrument collected spectroscopic data between 324 and 456 nm from $t = 36$ to 66 s, capturing peak heating.

II. Methodology

A. Flowfield

The method of analysis for the thermal protection system begins with computing the flowfield at discrete times along the EFT to sufficiently capture the heat pulse. Solutions were computed using the CFD code DPLR (Data Parallel Line Relaxation). The DPLR code is a parallel, multiblock, finite volume code that solves the reacting Navier–Stokes equations for continuum, including finite-rate chemistry and thermal nonequilibrium. The Euler fluxes are computed using modified Steger–Warming flux vector splitting [7] with third-order spatial accuracy via MUSCL extrapolation [8]. The viscous fluxes are computed to second-order accuracy using a central-difference approach. The flow is assumed to be laminar, in thermochemical nonequilibrium, and is modeled with a 2-temperature, 11-species, and 19-reaction finite-rate air chemistry model. The vibrational relaxation is modeled by the Landau–Teller formulation; relaxation times are obtained from Millikan and White [9], assuming simple harmonic oscillators, with the high-temperature correction of Park [10]. Rotational relaxation is modeled using the Parker model [11]. Viscous transport and thermal conductivity are modeled using the mixing rules by Gupta et al. [12]. The species diffusion coefficients are calculated with the bifurcation method [13], which has been shown to compare well with exact solutions of Stefan–Boltzmann equations. The surface of the heat shield is modeled with the radiative equilibrium boundary condition with a constant emissivity of 0.85. Because the emissivity does not change as the TPS would with charring, higher wall temperatures are likely.

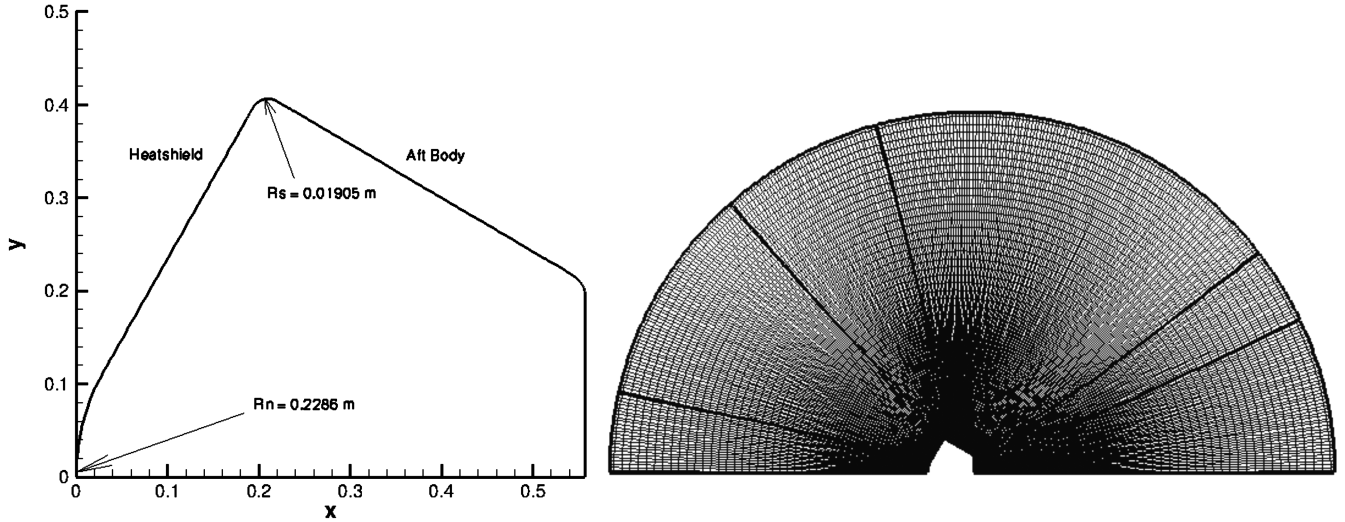

Fig. 1 The two-dimensional axisymmetric profile (left) and hyperbolic grid (right) used in the present Stardust postflight analysis. The axisymmetric profile corresponds to a 0.8-m-diam capsule, the nose R_n and the shoulder R_s radii are indicated. The hyperbolic grid is employed in the CFD simulations for the capsule surface. The grid index *i* increments circumferentially around the surface, and *j* increments radially outward.

Table 1 Time points from the 133 s EFT at which CFD solutions were generated

UT time	Time from entry, s	Altitude, km	Velocity, m/s	Density, kg/m^3	Temperature, K	Pressure, N/m^2	Notes
57:16.3	34	81.0	12,385.1	1.3e − 5	217.6	0.792	ECHELLE period
57:18.3	36	78.5	12,336.9	1.9e − 5	218.1	1.171	ECHELLE period
57:20.3	38	76.0	12,269.1	2.7e − 5	218.7	1.711	ECHELLE period
57:22.3	40	73.5	12,181.1	3.9e − 5	220.0	2.478	ECHELLE period
57:24.3	42	71.2	12,062.7	5.6e − 5	221.6	3.533	ECHELLE period
57:26.3	44	68.9	11,902.1	7.7e − 5	224.1	4.968	ECHELLE period
57:28.3	46	66.8	11,689.1	1.0e − 4	227.6	6.874	——
57:30.3	48	64.7	11,414.0	1.4e − 4	230.8	9.328	——
57:33.3	51	61.8	10,871.4	2.1e − 4	235.0	14.218	Peak heating
57:35.3	53	60.0	10,418.0	2.7e − 4	237.7	18.385	——
57:38.3	56	57.5	9,617.4	3.8e − 4	243.1	26.157	——
57:41.3	59	55.2	8,708.7	5.0e − 4	248.0	35.563	——
57:42.3	60	54.5	8,391.8	5.5e − 4	249.4	39.044	——
57:43.3	61	53.9	8,071.7	5.9e − 4	250.6	42.667	——
57:44.3	62	53.3	7,751.2	6.4e − 4	251.7	46.429	——
57:45.3	63	52.6	7,432.3	6.9e − 4	252.8	50.344	——
57:48.3	66	51.0	6,504.5	8.5e − 4	255.8	62.790	——
57:53.3	71	48.6	5,128.2	1.2e − 3	257.4	85.615	——
57:58.3	76	46.7	4,007.6	1.5e − 3	257.0	110.813	——
58:03.3	81	45.0	3,132.7	1.9e − 3	256.5	138.103	——
58:22.3	100	39.9	1,336.0	3.9e − 3	244.9	273.357	——

The wall catalysis is modeled using a constant catalytic efficiency of 1.0, and the wall was assumed to be fully catalytic to ions.

The assumption that Stardust was ballistic saves computational cost by allowing a two-dimensional axisymmetric grid, which is composed of 6 blocks and 43,000 grid cells. The grid was grown out hyperbolically (Fig. 1) in the body-normal direction to ensure orthogonality at the surface. As the solution converged on the hyperbolic grid, the grid was then adapted to the Mach contours to achieve proper grid alignment to the shock. A grid convergence study was performed and is summarized in Appendix A.

The aerothermal environment is constructed using a combination of CFD and engineering scaling relationships. Between CFD solutions, environments are linearly interpolated in time using the CFD results. At times before and after the CFD period, the environment is scaled by freestream velocity and density. Each surface point is scaled separately to provide heating-pulse continuity in time.

B. Material Response

The PICA material response along the Stardust EFT is modeled using the FIAT (version 2.4) code [14]. The 3.3 version of the PICA model is used in the present analysis [15]. The aerothermal environment (recovery enthalpy, pressure, and heat transfer coefficient) along the trajectory, as determined from CFD simulations, is input into FIAT. FIAT uses this information to define the convective and radiative heat fluxes at the surface. In the present analysis, the contribution from radiation originating from the shock layer to the PICA surface is not included because it accounts for less than 10% of the heat rate at peak heating, and surface heating is dominated by convection. Next, the surface energy balance equation that accounts for conduction, blowing, pyrolysis, and surface recession is solved. The material stack consists of PICA (5.8 cm), HT-424 (0.14 cm), and aluminum 2024 (1.27 cm). This model of FIAT employs a planar geometry assumption. All materials have an assumed initial temperature of −20°C. There is no contact resistance at any material interfaces and the back wall is assumed to be adiabatic. The material properties (heat capacity, thermal conductivity, and emissivity) of the material in the TPS stack are read from the FIAT material database. Heat capacity is modeled as a temperature-dependent quantity, and thermal conductivity varies with both pressure and temperature. For ablators, these material properties are separately listed for virgin and char materials. Within FIAT, the emissivity of PICA for both virgin and char is modeled as temperature-dependent and varies from 0.858 at 250 K to 0.93 at 3500 K.

The iteration between CFD and FIAT is loosely coupled. It is done by putting the surface temperature returned by FIAT back into the DPLR CFD code as a point-by-point isothermal boundary condition. Convergence of the loose coupling is met when the heat flux differences are negligible between the radiative equilibrium wall and the pointwise isothermal wall with temperature from FIAT. Another study, which looks specifically at the in-depth material and surface interactions, performed by Stackpoole et al. [16] compares the FIAT density profiles with the measured density profiles of cores taken from the heat shield of Stardust.

C. Observation

There was no onboard instrumentation on Stardust to record the reentry performance. The only temporally resolved data of the reentry are from the Stardust observation campaign [1]. A commercial miniature ECHELLE spectrograph was developed into a dedicated instrument to make optical spectroscopy available at high spectral resolution. The ECHELLE camera has a wavelength range of 368–872 nm (continuum emission is from 320–1450 nm wavelengths) and resolutions of 0.14 nm at 370 nm wavelengths to 0.9 nm at 880 nm wavelengths. The ECHELLE camera recorded 100 frames from $t = 34$ s [09:57:16.077 Universal Time (UT)] to $t = 44$ s (09:57:25.983 UT). This period of time is during the increase in heating before peak heating ($t = 51$ s, 09:57:33 UT). The reduction of the spectrographs needed to account for order overlap, window transmission, operating conditions, atmospheric extinction, and presence of emission lines. The flux is extracted and is used for comparison with the simulated data. Details of the camera and data reduction are given by Jenniskens and Sagan [2].

Computational results were compared and independently analyzed to near-UV spectra obtained with the SLIT telescope by Winter and Herdrich [3]. This instrument collected the light of the Stardust reentry with a small telescope and fed the light via an optical fiber to a rack-mounted SLIT spectrograph. The spectrograph obtained data in the wavelength range of 324 to 456 nm at 0.5 nm resolution. These spectra are dominated by the molecular bands of cyanide (CN), but they also contain continuum emission at the longer wavelengths. Tracking irregularities caused the signal to fluctuate, and only those times when the most light was collected into the optical fiber are considered.

A number of instruments provided a measure of flux from the Stardust SRC surface over the majority of the reentry. The near-infrared spectrograph (NIRSPEC) instrument by Taylor and Jenniskens [17] was a slitless spectrograph with a grism dispersion element placed in front of an InGaAs camera. It measured continuum emission at 930–1080 nm at 1.6 nm resolution. The spectra are dominated by continuum emission, just as in the visual wavelength range of ECHELLE. Because the spectra are dominated by the graybody emission, we also consider flux measurement obtained

with broadband imagers. Those include the pointing cameras for NIRSPEC (Xybion Electronic Systems) and an instrument called a high-frame-rate spectrograph (HFRS), operated by McHarg et al. [18] (low-light-level television), a digital imager camera (DIM) [19] from the aircraft, and a handheld camcorder, which observed the final part of the capsule's entry track from a site near Goshute Indian Reservation on the Utah–Nevada border. These instruments are generally more sensitive than the spectrographic cameras and can be calibrated directly to the background stars observed in the field.

III. Results

A. CFD Analysis

Stardust was modeled with DPLR as two-dimensional and axisymmetric. Each solution was run on 16 processors for approximately 6 h and required about three grid adaptions to properly align with the shock. Twenty-one solutions along the trajectory were computed to adequately capture the heat pulse and calculate the integrated heat load. The peak heat flux occurred at $t = 51$ s with a magnitude of 942 W/cm^2 at the stagnation point, and the integrated heat load at the stagnation point was 27.6 kJ/cm^2 (Fig. 2). In Fig. 3 the heat flux is plotted along the surface of the capsule for the heat shield and aftbody. The x axis is the horizontal distance from the stagnation point ($x = 0$). The peak of the heat flux is located at the stagnation point, as expected. The transition from the heat shield to the aftbody is seen around $x = 0.22$ m. The log plot shows the aftbody characteristics more clearly than the on the linear scale. Because of unsteady effects, there is not as much confidence in the solution on the aftbody as on the heat shield. A grid resolution study was unable to resolve this unsteadiness on the aftbody. The Mach contours and streamlines for the peak-heating case are shown in Fig. 4, in which flow is traveling from left to right. The final resulting adapted grid is shown in this figure. There is a very short standoff distance of the shock due to the high magnitude of velocity. A recirculation region is present directly behind the capsule. This figure illustrates that the aftbody is inherently unsteady and therefore difficult to resolve, because DPLR is not a time-accurate solver. The calculations made with the material response code and compared with the observation data include the heat shield only.

B. CFD and Material Response Coupling

Along the trajectory, a discrete number of CFD solutions were obtained. These solutions were interpolated in time along the trajectory. The following quantities were anchored with the CFD solutions and fit with engineering relationships for all other times in the trajectory. The heat transfer coefficient was scaled by ρV^3, surface pressure was scaled by ρ, and the freestream enthalpy was found with $V^2/2$, where ρ is freestream density and V is freestream velocity. These three quantities are the environment inputs to FIAT.

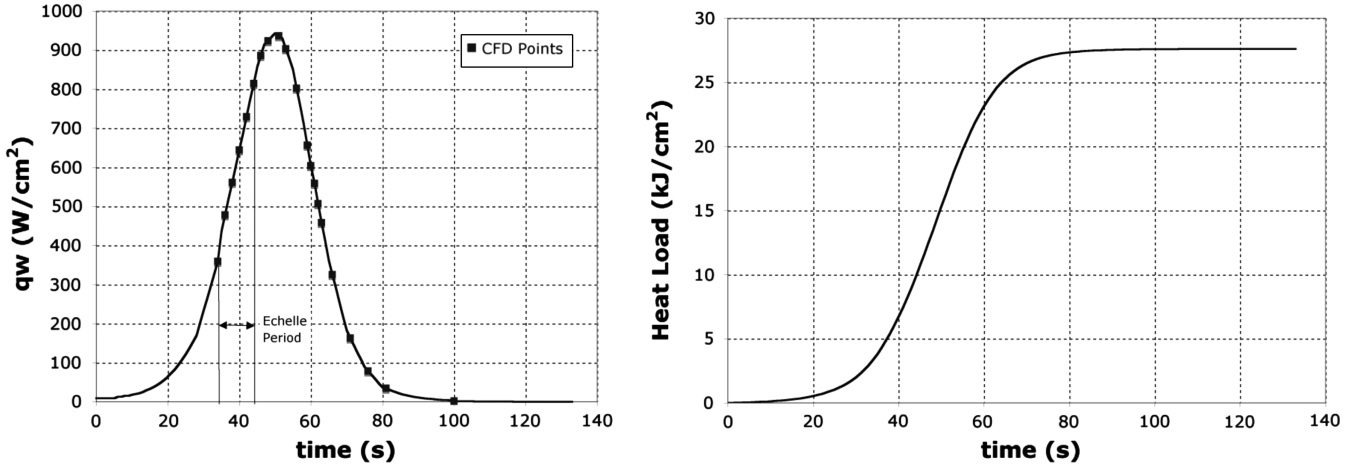

Fig. 2 Stagnation-point baseline convective surface heat flux (left) and integrated heat load (right). The squares on the heat flux curve represent the solutions generated from CFD. The line represents the interpolated data through these points. The integrated heat load has a value of 27.6 kJ/cm^2.

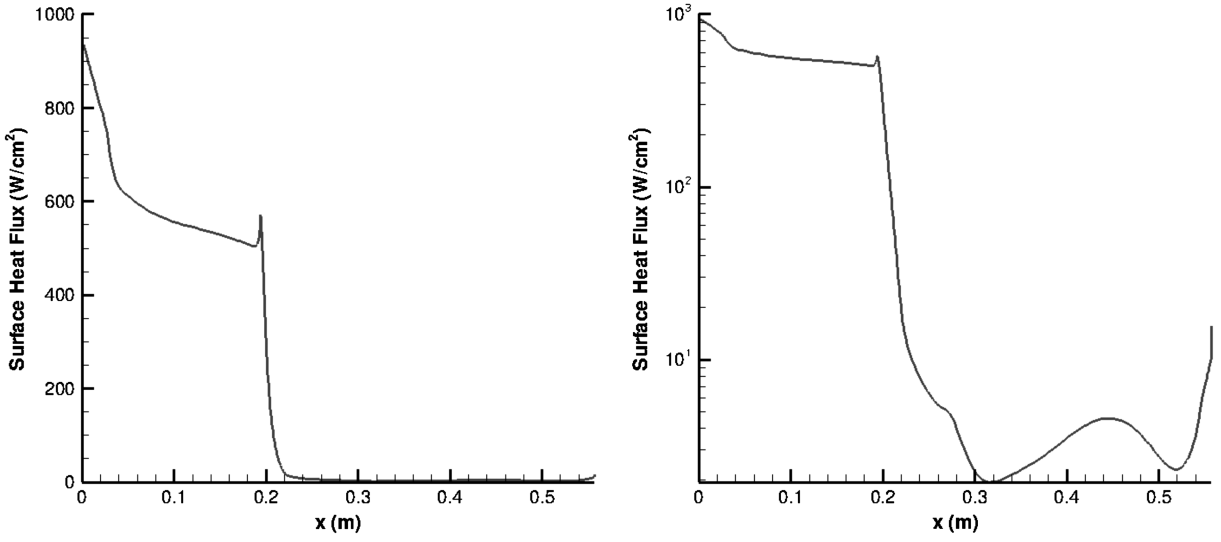

Fig. 3 The surface heat flux profile for the entire Stardust capsule at peak-heating time point (left). To show the results for the afterbody, the plot on the right shows the surface heat flux on a log scale.

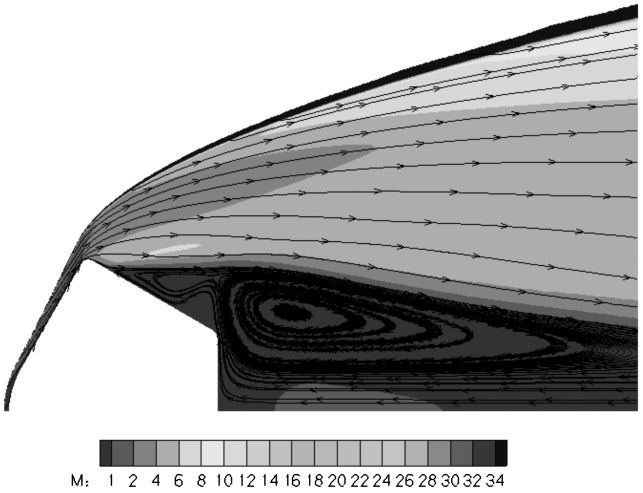

Fig. 4 Mach contours and streamlines for the baseline peak-heating case. The shock has a standoff distance of about 1.2 cm. This is a close-up view of the capsule region and does not display the entire computational domain.

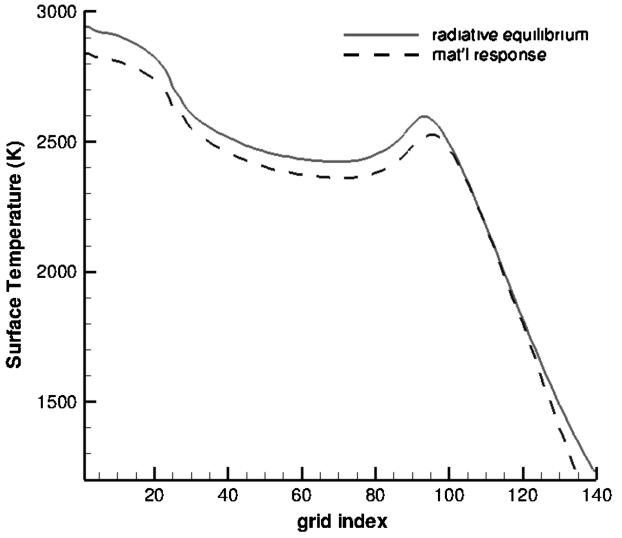

Fig. 5 Comparison of surface temperatures from radiative equilibrium (CFD) and material response (FIAT) at $t = 66$ s. Because the material response code accounts for ablation and conduction the corresponding surface temperature along the heat shield is 3% smaller but does not differ on the shoulder region. The grid index i runs along the surface of the heat shield.

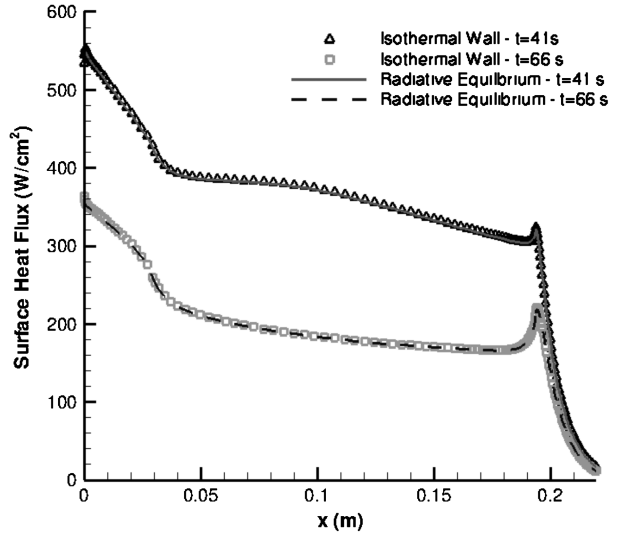

Fig. 6 Surface heat flux for the pointwise isothermal wall and radiative equilibrium wall boundary conditions at $t = 41$ and 66 s. The surface heat flux remains unchanged when isothermal wall boundary conditions are used and is indicative of the CFD's insensitivity to small changes in the wall temperature.

Although FIAT uses recovery enthalpy as an input, the freestream enthalpy is used here, because the two quantities are nearly equal and providing freestream enthalpy is simpler. A FIAT input was generated for each body point on the heat shield along the entire trajectory, which is 142 points on the baseline grid. The material response is simulated one-dimensionally in depth at each body point.

Two sets of data were generated for the surface temperature: one assuming radiative equilibrium and the other including the material response (isothermal wall). Radiative equilibrium assumes that all energy incident to the surface is reradiated to space as a function of emissivity and temperature raised to the fourth power. The wall temperature predicted by FIAT was then imposed as an isothermal boundary condition within the CFD solutions. The heating pulse from DPLR, calculated using the FIAT-generated surface temperature, is then input to FIAT for an update to the material response. This process is repeated until surface temperature and heat flux between DPLR and FIAT are converged. In practice, only one iteration is required. The surface temperature as a function of body points is output from the material response code several times in the trajectory. For two particular time points ($t = 41$ and 66 s) on the EFT, one on either side of the heat pulse, the surface temperature was output from FIAT at each body point of the heat shield. The surface temperature from the radiative equilibrium case and the surface temperature from the material response code at $t = 66$ s are shown in Fig. 5, in which the x axis is the grid index along the surface of the heat shield. The surface temperature from the material response code is about 97% of the DPLR surface temperature at its peak. Near the shoulder, there is remarkably good agreement between the radiative equilibrium case and the material response case, which could be due to the inaccurate planar geometry assumption made by the material response code. In Fig. 6 the heat flux for the two time points and each boundary condition is plotted. The differences in heat flux between the isothermal wall and radiative equilibrium wall are very minimal at each time point, despite a greater difference in the surface temperature. Because the difference in heat flux is negligible, no additional iterations between the CFD and the material response code were deemed necessary.

The procedures described previously are used to simulate the response of the heat shield through the entirety of the heat pulse. The final state of the material, characterized by its recession and in-depth density profile, is calculated. These calculations are compared with the recovered heat shield, as described by Stackpoole et al. [16].

C. Simulation and Observation Data Comparison

The ECHELLE camera captured spectral intensities of the Stardust reentry from $t = 34$ to 44 s. The ECHELLE data capture spectral emission resulting from the radiating surface and shock-layer emission. Shock-layer emission does not contribute much to the total spectral emission; therefore, spectral emission is a measure of surface temperature. These observational data were calibrated and averaged in time and represented as a graybody flux g to compare with the simulated data of the CFD and the material response code. By definition, a graybody is a blackbody with intensity B that accounts for emissivity ε:

$$g = \varepsilon B = \varepsilon \frac{2hc^2}{\lambda^5} \frac{1}{e^{hc/\lambda kT} - 1}$$

The heat-shield area is divided into finite elements, each with a unique surface temperature. The total flux is calculated as a sum of the contribution from all elements and as an average of all elements, taking into account the projected viewing angle of the capsule at any given moment in time. No correction for atmospheric extinction is

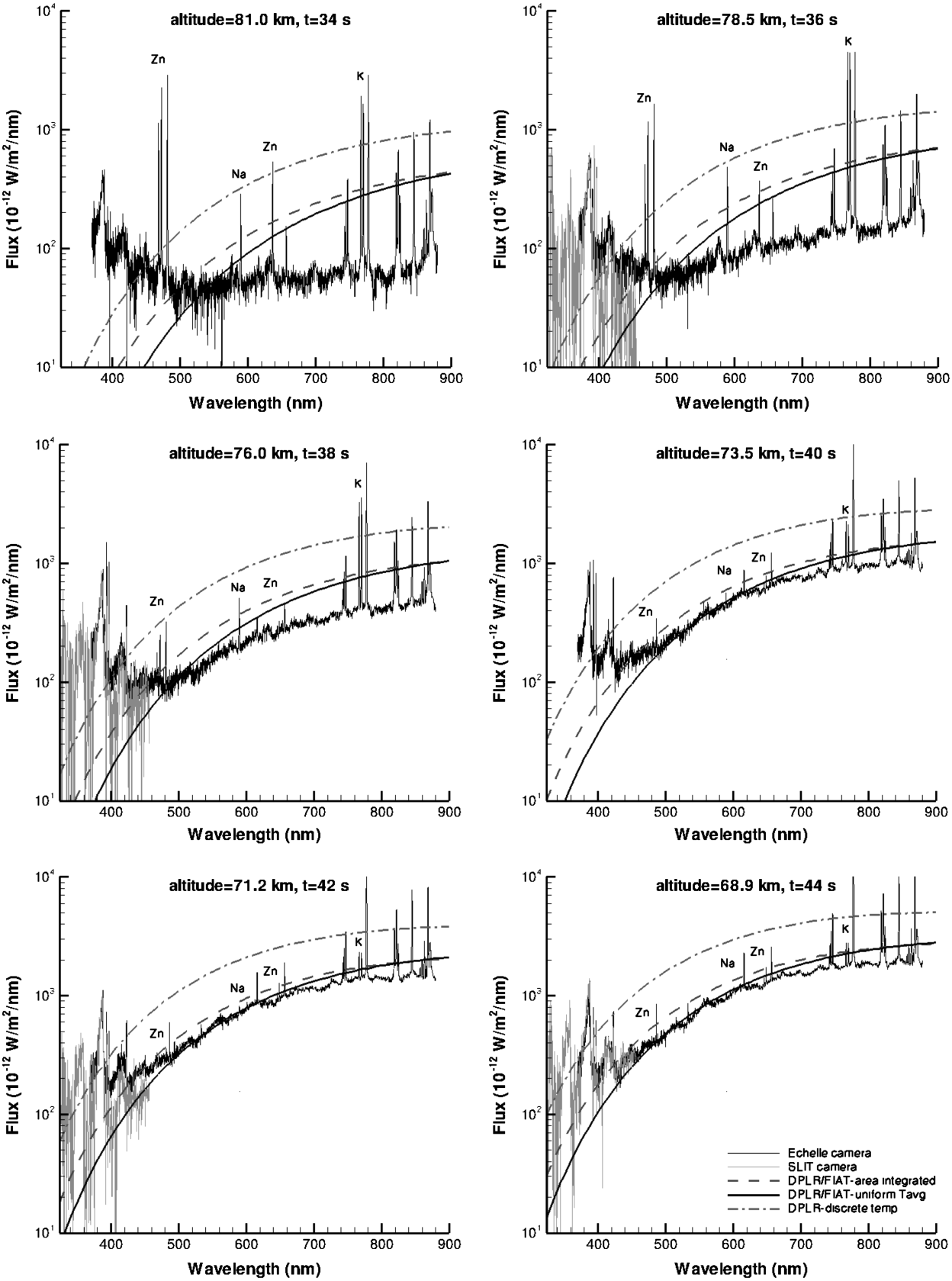

Fig. 7 Log scale of the graybody curves for radiative equilibrium CFD area-integrated, material response area-integrated, constant average temperature, and the ECHELLE and SLIT observational data. The material response code agrees well with the observational data, particularly at later times in the trajectory. The CFD, however, overpredicts throughout the entire ECHELLE period.

needed in the comparison because the observed data have already been corrected for it. Using the preceding equations, the simulated data were compared with the observed data. The CFD simulations assume an emissivity of 0.85; the material response code assumes emissivity changes with temperature and varies from 0.85 to 0.93. The graybody curve scales with emissivity.

Figure 7 shows the graybody plots of the radiative equilibrium case, material response case, and ECHELLE and SLIT data as

functions of wavelength. The emission lines result from the shock-layer emission. The ECHELLE data are point sources and have been corrected for atmosphere, view angle, and area by the square of the distance between the observation camera and the Stardust capsule. The simulated data are presented as graybody curves. The average surface temperature uses a graybody function with a surface average temperature. The area-averaged surface temperature is the superimposed graybody function of each radiating surface element at its local temperature. Because the graybody function is nonlinear, these two results are different. By looking at two different temperature distributions, the distribution effects can be considered with respect to the observation data, which has no spatial resolution.

IV. Discussion

Over the recording period of the ECHELLE camera, the graybody flux curves (Fig. 7) from the measurements and from the material response calculations (using area-integrated and average surface temperatures) show an excellent agreement, especially at later times. As expected, the area-integrated temperatures calculated based on the radiative equilibrium assumption (CFD) constantly overpredicts the material response graybody flux curves from 188 to 225%, and it relates to the earlier discussed differences in predicted surface temperatures (Fig. 5). As expected, with increasing heat flux (Fig. 2), the graybody curves will have an increased curvature toward longer wavelengths. This trend is observed in both recorded and simulated data. The largest discrepancy occurs at $t = 34$ s, when the ECHELLE flux curve seems to lack any graybody characteristics and instead exhibits a linear profile. The ECHELLE data at this time point are displaying CN bands, which are very strong and are intersecting the graybody flux curve at lower wavelengths, up to about 500 nm, making it appear linear.

The material response and CFD are, however, still overpredicting the ECHELLE data. At $t = 34$ s the flow is thought to be on the edge of the continuum/noncontinuum regimes. When comparing DPLR results with direct simulation Monte Carlo (DSMC) in [19], the DSMC found 13% lower heat flux than the CFD for $t = 34$ s of the Stardust trajectory. This difference in heating could explain some of the difference in the flux. Also, the Stardust capsule initially had a white thermal-control paint on the heat shield, composed of white ZnO pigment and a $KSiO_3$ binder. It is possible that the overprediction of surface temperatures is due to the modeling not including effects of the paint. The discrepancy coincides in time with high-emission intensity in lines attributed to paint products. The paint products are identified as potassium (K), sodium (Na), and zinc (Zn). As the paint product emission lines fade in time, the paint is ablating away, $t = 36$ to 40 s, the surface temperature prediction begins to agree with the observed temperature.

At later time points, $t = 40$ to 44 s, the material response case is agreeing well with the ECHELLE data. The material response case is more physically representative of Stardust because it accounts for recession, charring, density variations, and, most important, ablation in the surface temperature prediction. As seen in Fig. 5, the material response surface temperature is lower than the radiative equilibrium predicted surface temperature. By adjusting the material response surface temperature by 50 K for the area-integrated temperature assumption, the constant surface temperature assumption bounds the ECHELLE data. This suggests that the surface temperature can be predicted through material response to within 50 K.

The surface temperature distribution assumption has an effect on the graybody flux curve as well. The material response area-integrated temperature assumption has a steeper-slope flux curve between 320 and about 700 nm wavelengths than the material response constant-average-temperature assumption. The ECHELLE data's best fit is somewhere in the middle. In Fig. 8 a temperature range of ± 50 K of the CFD and material response modeling predictions is plotted with ECHELLE and SLIT instruments. In the wavelength range of 400 to 700 nm, the spectral observation data are well bounded by the computational temperature window.

To investigate the surface temperature over a larger range in altitudes, the results were first compared with broadband flux

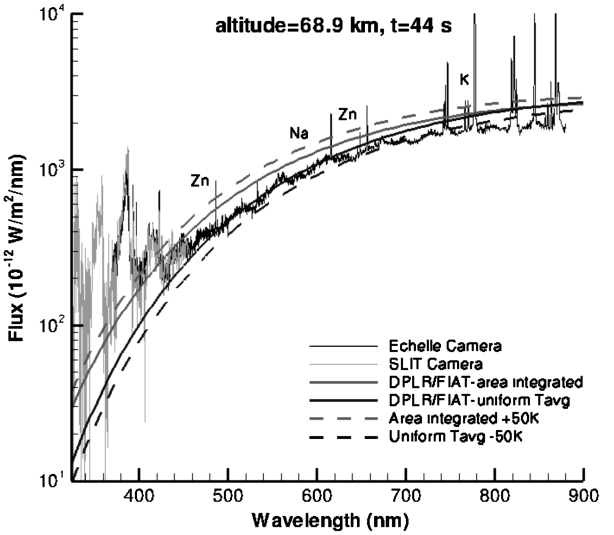

Fig. 8 Material response area-integrated surface temperature adjusted for an increase of 50 K and the material response constant average surface temperature adjusted for a decrease of 50 K. The adjusted temperature ranges now bound the ECHELLE data.

measurements with the DIM by Jenniskens and Wercinski [19], the intensified Xybion camera by Taylor and Jenniskens [17], which was the pointing camera for NIRSPEC, a low-light-level pointing camera for the HFRS by McHarg et al. [18], and those obtained with a handheld video on the ground. These data are plotted in Fig. 9. Because most of the broadband emission is from continuum radiation, the temperature profile over the forebody of Stardust (and the corresponding graybody spectra) is used to derive the flux at 548 nm from that measured over a wider wavelength range. In addition, Fig. 9 includes the continuum emission at 1013 nm measured by the NIRSPEC instrument [17], translated in the same manner to 548 nm, and that measured directly at 548 nm by the INT1 instrument [20]. All data are corrected for atmospheric extinction, then normalized to a standard distance of 100 km between capsule and observer. The material response results, especially the temperature-averaged data, provide a good fit to the observations.

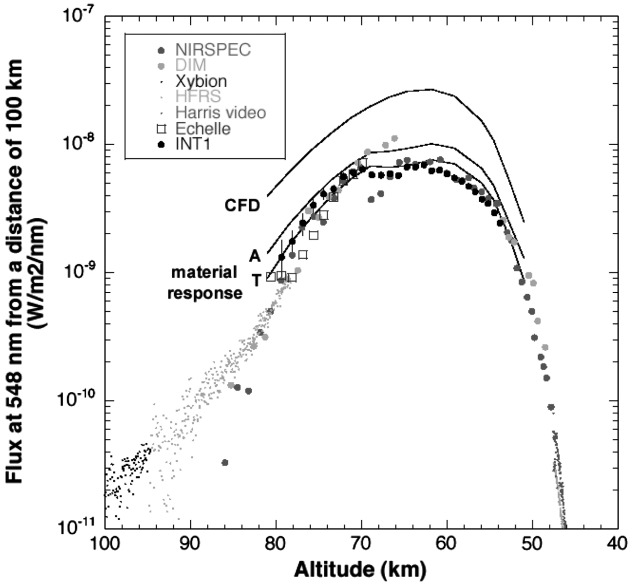

Fig. 9 Apparent flux of the sample return capsule at wavelength 548 nm as seen from the aircraft, normalized to a unit distance of 100 km. The measurements from several instruments (see legend) are compared with CFD and material response model predictions.

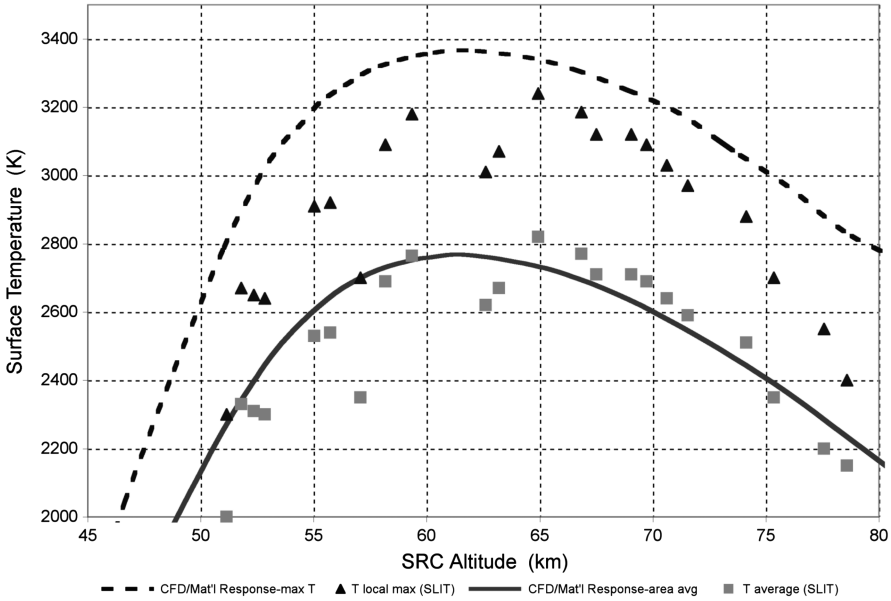

Fig. 10 Average surface temperature from the radiative equilibrium wall assumption and the material response case compared with surface temperatures obtained from the SLIT telescope [21] with linear distribution and constant-temperature assumptions.

A small discrepancy may exist around 60 km altitude, when the observed flux is 19% lower. In Fig. 9 the CFD/material response area-integrated solution is denoted as *A*, the CFD/material response uniform average surface temperature is denoted as *T*, and the radiative equilibrium wall without material response coupling is CFD.

The results of this reentry simulation are compared with the temperatures independently derived from the analysis presented by Winter and Herdrich [3] (Fig. 10). As part of the same observation, Winter and Herdrich obtained spectra using the SLIT telescope for a wavelength range of 324 to 456 nm. This instrument captured approximately 30 s of flight around the maximum heating point, from $t = 36$ to 66 s. The broadband spectra are compared in Fig. 7 with the ECHELLE spectra. The SLIT telescope obtained surface temperatures based on a simplified temperature distribution derived from the CFD simulations on the surface [21], because the SLIT, like all the instruments aboard the DC-8, had no spatial resolution. Through this distribution assumption, a local peak temperature was found. An average surface temperature was also found. The average temperature distribution assumption yields the lower limit of the surface temperature range, and the peak temperature provides the upper limit. These temperatures are compared with the average and maximum surface temperatures obtained from the CFD/material response case (Fig. 10). The average surface temperatures compare very well. The maximum temperatures are higher for the CFD/material response than for SLIT. The CFD/material response average temperatures agree with the SLIT average temperature to as close as 1 to 5% at its peak difference. The higher predictions at altitudes 75 km and above are related to the overpredictions seen in the ECHELLE data and are possibly related to the presence of paint.

V. Conclusions

The Stardust sample return capsule had the fastest Earth reentry of an artificial vehicle. The flight of Stardust is an important flight-test case for the phenolic impregnated carbon ablator heat shield and the extreme environments it returned in for the design of the crew exploration vehicle and the aerothermal community. The present study applied CFD simulations and material response predictions to the Stardust trajectory and compared the results with spectral observation data to assess the surface temperature during reentry.

The CFD solutions showed a peak-heating value of 942 W/cm^2 at 51 s after reentry and a heat load of 27.6 kJ/cm^2. The CFD environment was passed on to the material response code, which gave a corresponding surface temperature, accounting for conduction, blowing, pyrolysis, and surface recession or ablation. The pointwise surface temperature from the material response code was then used as an isothermal boundary condition within the CFD. The resulting heat flux differed by only 1% from the heat flux found with the radiative equilibrium wall boundary condition, indicating that the solution between the CFD and the material response code was converged and that CFD is insensitive to small changes in surface temperature.

The surface temperature obtained from the coupling of CFD and material response code is compared against spectral observation data from the ECHELLE and SLIT instruments [22] via graybody flux curves. Overall, the calculated and measured data exhibit excellent agreement for altitudes of 75 to 70 km, especially with the surface temperatures predicted via material response, which can be accurately predicted within ± 50 K for later time points.

The temperature distribution assumption on the heat shield has a direct effect on the flux. Both average surface and area-integrated surface temperatures reproduce the ECHELLE data for most of the spectra (450 to 900 nm). For the shorter wavelengths, 450 nm and below, the area-integrated surface temperatures from the material response code seem to better match the slope of the measured spectra yet give higher flux. Consistent with the SLIT observation, this is indicative of the fact that the temperature distribution on the heat shield needs to be taken into account. A discrete temperature area integration captures the behavior of the observational data best.

Above 75 km, there is an overprediction of surface temperature that is coincident with strong zinc and potassium emission, indicative of an ablating-white-paint layer not included in the model. The ablating paint cools the surface. As the paint ablates away, the surface temperatures are predicted very well.

The iterative methodology of coupling CFD (DPLR) with material response (FIAT) employed in the present paper proves to be a reliable tool to predict surface temperatures. Because surface temperature is one of the critical parameters as an indicator of the material performance used in the design and sizing of thermal protection systems, the results presented in this paper increase the reliability of such a combined CFD and material response approach for future missions, such as CEV.

Appendix A

Grid Study

To ensure proper grid convergence of the CFD solutions, a grid study was performed at the peak-heating condition. The baseline grid

Table A1 Comparison of heat-shield grid density in the baseline and fine grids, in which *i* increments along the surface and *j* is in the body-normal direction

	Baseline		Fine grid		
Block	*i*	*j*	*i*	*j*	
1	24	128	48	132	Stagnation region
2	64	128	128	132	Flank
3	48	128	256	132	Shoulder

used for these calculations was composed of six blocks; blocks 1 through 3 comprise the heat shield, with dimensions listed in Table A1. The surface of the capsule is defined by *i* and the body-normal direction is denoted as *j*. The fine grid is a denser grid with grid points relocated. The shoulder-region density is increased by a larger amount than other parts of the heat shield to see how the resolution around the corner would affect the solution. The shoulder is important to consider because it is sensitive to the flow due to the change in geometry and because the material response code assumes planar geometry, which it clearly is not. The body-normal grid density was also increased. The baseline and fine grids are shown in Fig. A1, in which the baseline is on the top and the fine grid is on the bottom.

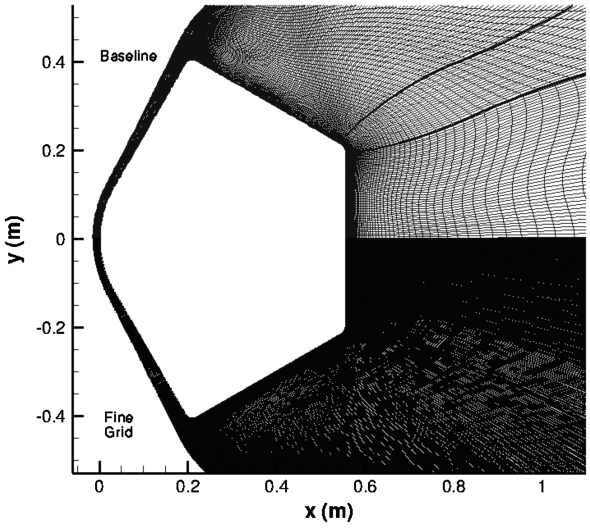

Fig. A1 Comparison of the baseline (top) and fine grid (bottom) in the pitch plane, which illustrates the grid adaption and wake region. The grid points were relocated, as well as increased, to better resolve the shoulder.

Although the fine grid is denser than the baseline, it also had a quick convergence, but it was run on 30 processors instead of 16. The baseline and fine grids were adapted independently; the fine grid required five grid adaptions to be performed. Standard practice for determining grid convergence includes agreement on the flowfield temperature and the surface heat flux. Figure A2 shows the temperature contours in the flowfield and the temperature along the stagnation line for each grid. The temperature contours between the two grids match up quite well. The stagnation-line plot of temperature confirms that the flowfield between the two grids is comparable. The peak temperature at the shock in the fine grid is slightly higher than the baseline grid by about 4.7%. The location directly at the shock would expectedly be the most sensitive to the grid density and shape. The temperature agrees at most other locations on the stagnation line and the peak difference is below the typical acceptance value of 5%. The surface quality of the grids is evaluated through the temperature and heat flux (Fig. A3), which is very dependent upon the grid. The temperature and heat flux on the surface of the fine grid is nearly identical to that on the baseline grid. Because there is agreement in the shock region and on the surface between the baseline and fine grids, it can be assumed that the baseline grid is converged.

Acknowledgments

This work was funded and managed by the Orion Thermal Protection System Advanced Development Project and the NASA Engineering and Safety Center. Part of the work for the present paper was supported by contracts from NASA Ames Research Center: NNA04BC25C to ELORET and NNA06CA84A to SETI Institute. Contributions by Dean Kontinos, David Hash, Deepak Bose, Mairead Stackpoole, and Michael Wright with technical advice or comments on the present manuscript are acknowledged. Jim Albers retrieved the broadband data from the video records. We thank Tim Harris for making his video record available for analysis, Mike Taylor for making the Xybion imaging available for analysis, and Geoff McHarg for making the low-light-level TV camera data available. NASA's DC-8 Airborne Laboratory was deployed by the University of North Dakota and Naval Systems Engineering Resource Center, under contract with NASA Wallops Flight Center.

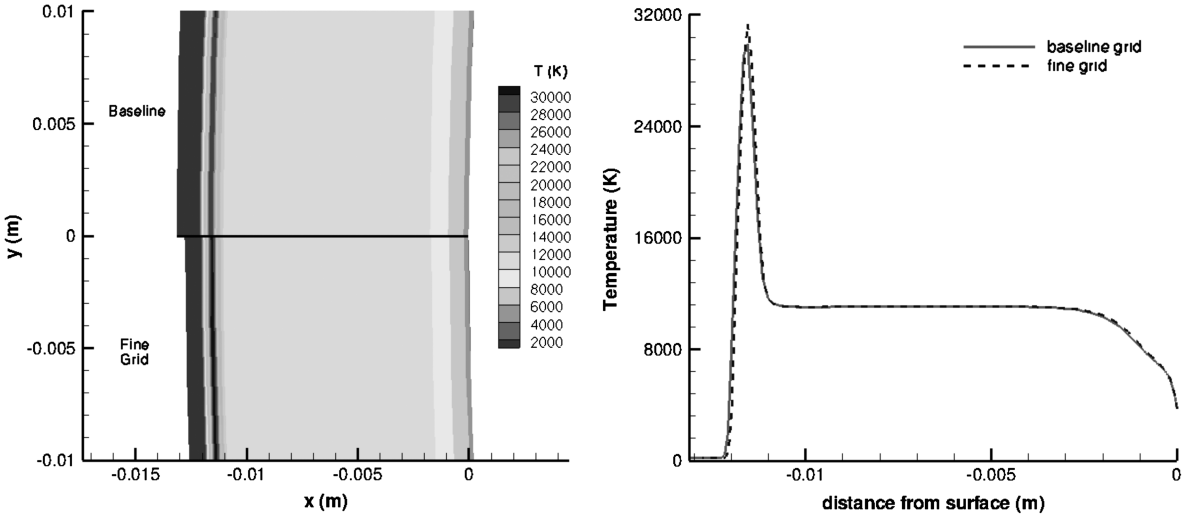

Fig. A2 Temperature contours in the flowfield (left) and temperature along the stagnation line in the flowfield (right) for the baseline and fine grids. Differences in the boundaries are attributed to independent adaptions. The maximum temperature difference falls within an acceptable 5%.

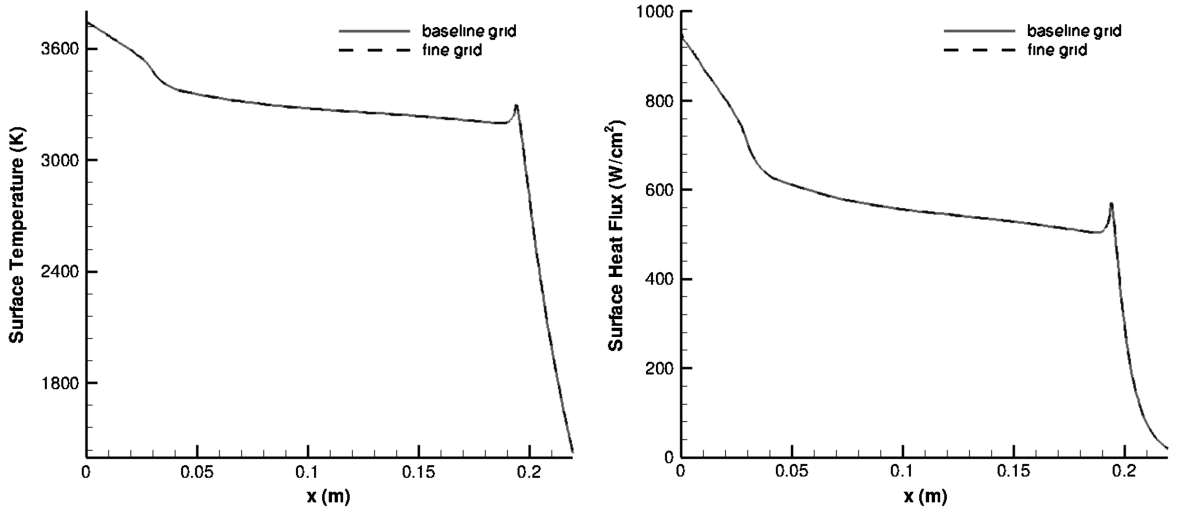

Fig. A3 Surface temperature (left) and surface heat flux (right) on the heat shield for the baseline and fine grids at peak heating. These surface quantities for the baseline and fine grids are nearly equal. Because there is such good agreement between the two grids, the baseline grid has been deemed to be converged.

References

[1] "Stardust Hypervelocity Entry Observing Campaign Support," NASA Engineering and Safety Center Rept. RP-06-80, 31 Aug. 2006.

[2] Jenniskens, P., and Sagan, C., "Observations of the Stardust Sample Return Capsule Entry with a Slit-Less Echelle Spectrograph," AIAA Paper 2008-1210, Reno, NV, Jan. 2008.

[3] Winter, M., and Herdrich, G., "Spectroscopic Observation of the Stardust Re-Entry in the Near UV," AIAA Paper 2007-4050, Miami, FL, June 2007.

[4] Wright, M., Candler, G., and Bose, D., "Data-Parallel Line Relaxation Method for the Navier–Stokes Equations," *AIAA Journal*, Vol. 36, No. 9, 1998, pp. 1603–1609. doi:10.2514/2.586

[5] Chen, Y.-K., and Milos, F. S., "Fully Implicit Ablation and Thermal Analysis Program (FIAT)," *Fourth International Conference on Composites Engineering (ICCE/4)*, edited by D. Hui, International Community for Composites Engineering and College of Engineering, Univ. of New Orleans, New Orleans, LA, 1997, pp. 661, 662.

[6] Desai, P., Qualls, G., and Levit, C., "Stardust Entry Reconstruction," AIAA Paper 2008-1198, Reno, NV, Jan. 2008.

[7] MacCormack, R., and Candler, G., "The Solution of the Navier–Stokes Equations Using Gauss-Seidel Line Relaxation," *Computers and Fluids*, Vol. 17, No. 1, 1989, pp. 135–150. doi:10.1016/0045-7930(89)90012-1

[8] Yee, H., "A Class of High-Resolution Explicit and Implicit Shock Capturing Methods," NASA TM 101088, Feb. 1989.

[9] Millikan, R., and White, D., "Systematics of Vibrational Relaxation," *Journal of Chemical Physics*, Vol. 39, No. 12, 1963, pp. 3209–3213. doi:10.1063/1.1734182

[10] Park, C., *Nonequilibrium Hypersonic Aerothermodynamics*, Wiley, New York, 1990.

[11] Parker, J. G., "Rotational and Vibrational Relaxation in Diatomic Gases," *Physics of Fluids*, Vol. 2, 1959, pp. 449–462.

[12] Gupta, R., Yos, J., Thompson, R., and Lee, K., "A Review of Reaction Rates and Thermodynamic and Transport Properties for an 11-Species Air Model for Chemical and Thermal Nonequilibrium Calculations to 30000 K," NASA RP-1232, Aug. 1990.

[13] Bartlett, E. P., Kendal, R. M., and Rindal, R. A., "An Analysis of the Coupled Chemically Reacting Boundary Layer and Charring Ablator: Part 4: A Unified Approximation for Mixture Transport Properties for Multi-Component Boundary-Layer Applications," NASA CR-1063, June 1968.

[14] Milos, F. S., Chen, Y.-K., and Squire, T. H., "Updated Ablation and Thermal Response Program for Spacecraft Heat Shield Analysis," 17th Thermal and Fluids Analysis Workshop, Univ. of Maryland, Paper TFAWS06-1008, Aug. 2006.

[15] Milos, F. S., and Chen, Y.-K., "Two-Dimensional Ablation, Thermal Response and Sizing Program for Charring Ablators," 46th AIAA Aerospace Sciences Meeting, AIAA Paper 2008-1223, Jan. 2008.

[16] Stackpoole, M., Sepka, S., and Kontinos, D., "Post-Flight Evaluation of Stardust Sample Return Capsule Forebody Heat Shield Material," AIAA Paper 2008-1202, Reno, NV, Jan. 2008.

[17] Taylor, M. J., and Jenniskens, P., "Near-IR Spectroscopy of the STARDUST Sample Return Capsule Entry: Detection of Carbon," *Journal of Spacecraft and Rockets* (to be published).

[18] McHarg, M. G., Stenbaek-Nielsen, H. C., and Kammae, T., "Observations of the Stardust Sample Return Capsule Entry Using a High Frame Rate Slit-Less Spectrograph," *Journal of Spacecraft and Rockets* (submitted for publication).

[19] Jenniskens, P., and Wercinski, P., "Digital Still Snapshots of the Stardust Sample Return Capsule Entry," *Journal of Spacecraft and Rockets* (to be published).

[20] Jenniskens, P., Albers, J., and Koop, M., "Low-Resolution Optical Spectroscopy of the Stardust Sample Return Capsule Entry with the INT1 Instrument," *Journal of Spacecraft and Rockets* (to be published).

[21] Winter, M., and Trumble, K., "Spectroscopic Observation of the Stardust Re-Entry in the Near UV with SLIT: Deduction of Surface Temperatures and Plasma Radiation," *Journal of Spacecraft and Rockets* (to be published).

[22] Jenniskens, P., Wercinski, P. F., Olejniczak, J., Wright, M., Raiche, G., Kontinos, D., Desai, P. N., Spalding, R. E., Sandquist, K., Rossano, G., Russell, R. W., Revelle, D. O., Hladiuk, D., and Hildebrand, A. R., "Surface Heating from Remote Sensing of the Hypervelocity Entry of the NASA Genesis Sample Return Capsule," AIAA Paper 2006-0381, Reno, NV, Jan. 2006.

M. Wright
Guest Editor